JACS
JOURNAL OF THE AMERICAN CHEMICAL SOCIETY

Article

pubs.acs.org/JACS

Chemical Pathways Connecting Lead(II) Iodide and Perovskite via Polymeric Plumbate(II) Fiber

Yunlong Guo, Kazutaka Shoyama, Wataru Sato, Yutaka Matsuo, Kento Inoue, Koji Harano, Chao Liu, Hideyuki Tanaka, and Eiichi Nakamura*

Department of Chemistry, The University of Tokyo 7-3-1 Hongo, Bunkyo-ku, Tokyo 113-0033, Japan

Supporting Information

ABSTRACT: Despite tremendous progress in optoelectronic devices using lead perovskite ($CH_3NH_3^+PbI_3^-$), there has been a paucity of mechanistic information on how photoactive micron-sized crystals of lead perovskite grow from a mixture of a layered crystal of lead(II) iodide and methylammonium iodide mediated by a polar solvent, DMSO or DMF. We report here that the whole process of the lead perovskite synthesis consists of a series of equilibria driven by reversible solvent participation involving a polymeric strip of plumbate(II) oligomer as a key intermediate. A significant finding includes quick decomposition of perovskite crystal upon exposure to DMSO or DMF at room temperature, where the solvent molecules act as a base to remove acidic ammonium iodide from the perovskite crystal. This observation accounts for the difficulty in controlling perovskite solar cell fabrication. Overall, the polar solvent is indispensible first to degrade a 2-D sheet of crystals of lead(II) iodide into 1-D fibrous intermediates and then to promote Oswald ripening of perovskite crystals. The detailed chemical information provided here will help to rationalize the photovoltaic device studies that have so far remained empirical and to open a new venue to a developing field of microscale lead perovskite devices, as illustrated by fabrication of photovoltaic devices and photodetectors.

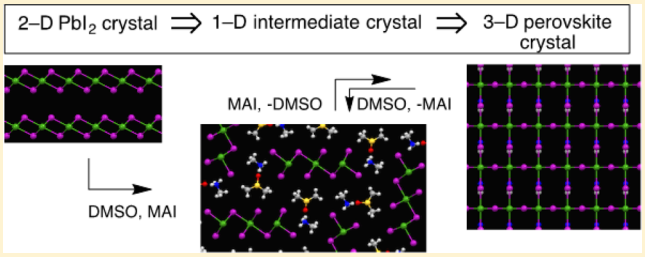

INTRODUCTION

Development of solar cell (SC) devices using lead perovskite ($CH_3NH_3^+PbI_3^-$; $MA^+PbI_3^-$; **PV**)[1−9] revitalized the research on materials morphology,[10] e.g., large crystals[11] and one-dimensional (1-D) fibers,[6,12−14] both of which have been observed during conversion of a mixture of $(PbI_2)_n$ (**PI**) and $CH_3NH_3^+I^-$ (MAI) to **PV**[15,16] mediated by DMSO or DMF. However, the chemical origin of this diversity of morphology has been unknown, unlike similar organic fiber materials on which some studies have been reported.[17] We thus became intrigued by the reaction pathway, where a two-dimensional (2-D) crystal of **PI** is converted to a three-dimensional (3-D) cubic lattice of **PV** (Figure 1). We have isolated some new fibrous 1-D crystalline intermediates in the **PI**-to-**PV** conversion and determined their crystal structure. Here we report that 1-D fibrous intermediates lie in the middle of the whole equilibrium and connect a **PI** sheet and a large **PV** cubic crystal through reversible participation of the polar solvent molecules (Figure 2a−f). The equilibrium is mobile in the presence of MAI and solvent at 30−100 °C, faster in DMF than in DMSO, but stops at the **PV** stage when solvent is lost while MAI is retained. For instance, a fibrous plumbate, **INT-3**, synthesized in DMSO (Figure 2g) loses solvent molecules at 100 °C to produce **PV** as a crystalline fiber (Figure 2h), which is stable if solvent-free. However, it goes back quickly to **INT-3** at room temperature upon exposure to solvent vapor, because the solvent molecules act as a base to remove MAI molecules from the **PV** crystal. This process accounts for the growth of 1-D fibers to large crystals via Ostwald ripening (Figure 2i,j). It also accounts for the well-known difficulty in controlling solar

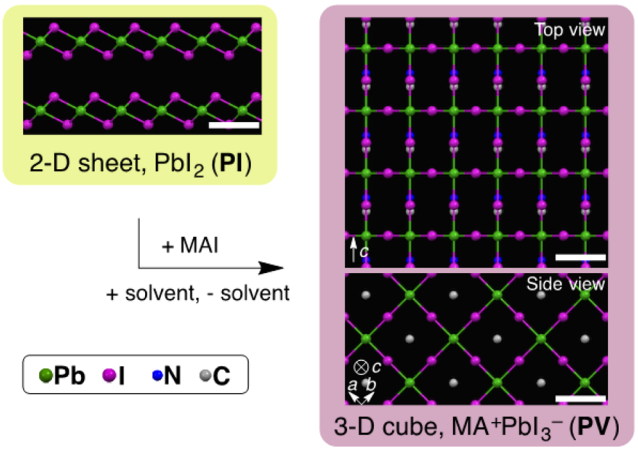

Figure 1. **PI**-to-**PV** conversion mediated by DMSO or DMF, which accompanies significant dislocation of atoms. Crystallographic structures of **PI** and **PV** (seen along two orthogonal directions). The scale bars are 0.5 nm.

Received: October 9, 2015
Published: November 29, 2015

DOI: 10.1021/jacs.5b10599
J. Am. Chem. Soc. 2015, 137, 15907−15914

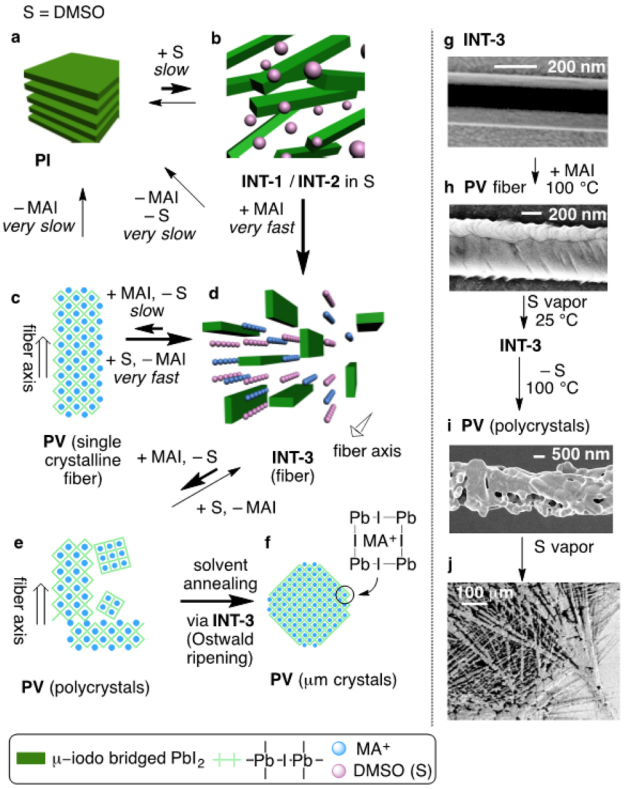

Figure 2. Pathways of **PI**-to-**PV** conversion mediated by DMSO. Productive pathways in the solution-processed SC fabrication are shown as bold arrows. (a–f) Conversion of sheets of **PI** to cubic crystals of **PV** in DMSO. (g) Low-landing-voltage scanning electron microscopic (SEM) image of **INT-3**. (h) SEM image of **PV** obtained after heating **INT-3** at 100 °C. (i) SEM image of polycrystalline **PV** after one solvent annealing cycle. (j) **PV** crystal network formed after Ostwald ripening.

cell fabrication, an adverse effect. The single crystalline **PV** nanofiber obtained by the use of DMSO (Figure 2h) allowed us to fabricate microscale photovoltaic devices and photodetectors that show performance comparable to that of single-block crystal device.[11,18] The high performance of these devices attests to the value of the mechanistic insights for the development of miniature devices and for the study of the optoelectronic properties of **PV** materials.

RESULTS AND DISCUSSION

Solvent Effects on Chemical Pathways of Perovskite Formation. We first synthesized and isolated the intermediates **INT-1**–**3**, **-6**, and **-7** (Figure 3; all except **INT-1** were obtained as micron-sized fibers), occurring under the conditions of the standard SC device fabrication, as described in the Experimental Section (a 30–50 wt % **PI** and MAI solution in DMSO or DMF heated at 60 °C). The compounds in red boxes were characterized by single crystal X-ray crystallographic analysis for the first time in this work (**INT-2** and **-3**) or previously (**INT-1**,[19] **-6**,[20] and **-7**[21]), and those in blue boxes (**INT-4** and **-5**) were identified by in situ X-ray diffraction (XRD) in this work [Figure S1–S3, Supporting Information (SI)]. Figure 3 summarizes their reactions as revealed by in situ 2-D XRD analysis of a sample held on a loop (cf. Figure 3b). Scanning electron microscopic (SEM) images supplemented the XRD crystallographic information.

The reaction mediated by DMF (Figure 3c) is mechanistically simpler than the DMSO-mediated reaction and described first. A mixture of **PI** and MAI in hot DMF directly produces a key intermediate, a dinuclear plumbate (i.e., $Pb^{II}I_3^-$)[22,23] isolated as a crystalline fiber [**INT-7**, $(MA^+)_2(PbI_3^-)_2{\cdot}DMF_2$, step xvi], which easily loses DMF to produce a **PV** fiber ($MA^+PbI_3^-$) under nitrogen at 20–100 °C (step xviii). This **PV** fiber is brittle and fractured, as seen by SEM (Figure 3d). The formation of **INT-7** from **PI** was found to occur in two steps: First, exfoliation and truncation of a 2-D sheet of **PI** in hot DMF give reversibly a polymer strip of neutral $(PbI_2)_2$ (**INT-6**, crystalline fiber, steps xv and xxi). Second, supply of MAI by surface coating of **INT-6** results in rapid ligand exchange at 25 °C to give **INT-7** (step xvii). The **PV** fiber is stable at 100 °C under nitrogen, but regenerates **PI** at >130 °C by loss of MAI (step xx). Notably, under DMF vapor, the **PV** fiber spontaneously regenerates **INT-7** at 25 °C within 0.5 h (step xix); that is, the DMF molecules act as a base to extract acidic MAI molecules out of the PbI_3^- crystal lattice, and PbI_3^- is converted to the dinuclear cluster **INT-7**. This process will be discussed later for Figure 4, where $MA^+{\cdot}$DMF hydrogen-bonding interaction is illustrated.

The DMSO reaction is similar to the DMF reaction except for a few important details (Figure 3a). A mixture of **PI** and MAI in hot DMSO produces a new class of trinuclear plumbate as fibers [**INT-3**, $(MA^+)_2[(PbI_3^-)_2PbI_2]{\cdot}DMSO_2$, step iii]. The very smooth surface of the fibers is notable (Figure 2g). The structure was determined by single crystal analysis (Figure 4d,e). Drop-casting on ITO and slow evaporation of the same mixture of **PI** and MAI in DMSO also produces the **INT-3** fibers (Figure S4, SI). An entity that shows the same XRD pattern as **INT-3** was previously assigned to be $MA^+PbI_3^-{\cdot}$DMSO on the basis of elemental analysis.[24] **INT-3** also forms in two steps from **PI**: **INT-1** and **INT-2** are synthesized under reaction conditions with subtle difference (see the Experimental Section; steps i and ii, as well as xii and xiii). When coated with MAI, mononuclear **INT-1** gives trinuclear **INT-3** within 30 s at 25 °C (step iv), while dinuclear **INT-2** gives it more slowly (step v).

Because **INT-3** $[(PbI_3^-)_2PbI_2]$ needs one additional MAI molecule to make **PV** $[3(PbI_3^-)]$, heating at 100 °C produces a 1:2 mixture of **PI** and **PV** (step vi). When **INT-3** fibers are coated with MAI, intrusion of MAI into the fibers occurs to produce **INT-4**, followed by loss of two DMSO molecules to produce **PV** via **INT-5** (steps vii–ix). **INT-4** and **INT-5** were identified by 2-D XRD analysis (vide infra). The **PV** fiber produced in this way from **INT-3** is highly crystalline, as supported by SEM (Figure 2h), XRD, and selected-area electron diffraction (SAED) of the fiber (Figure S5, SI). The **INT-3**-to-**PV** conversion accompanies mechanical stiffening of the fiber and a color change from yellow to black with a ratio of Pb:I = 1:3 (Figures S6 and S7, SI). Like DMF, DMSO vapor quickly extracts MAI to convert **PV** fiber into **INT-3** fiber at 25 °C (step x). The interconversion between **PV** and **INT-3** is so fast that exposure of the crystalline **PV** fibers to DMSO vapor at 25 °C causes quick degradation of the fiber to powder via **INT-3**, followed by Ostwald ripening of crystals, as seen in the SEM images in Figure 2g–j.

Single Crystal Structure Analysis of Intermediates. Figure 4a–e,j,k shows the crystal structures of **PI**,[25] **INT-1**,[19] **-2**, **-3**, **-6**,[20] and **-7**[21] as viewed approximately along the $(PbI_2)_n$ polymer chains (only two sets of Pb atoms are shown for clarity). All of these structures have in common a μ-iodo-

DOI: 10.1021/jacs.5b10599
J. Am. Chem. Soc. 2015, 137, 15907–15914

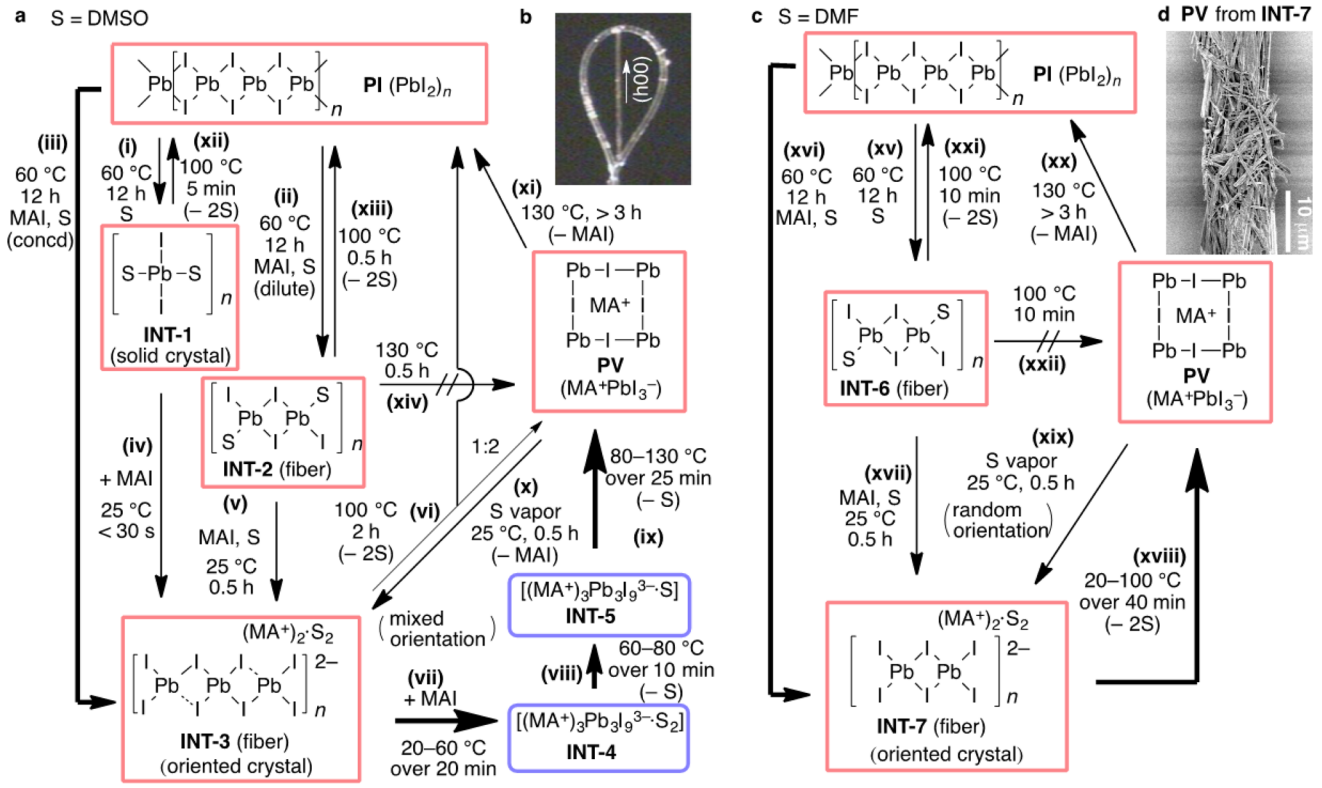

Figure 3. Chemical reactions between **PI** and **PV** mediated by DMSO or DMF studied for isolated crystalline intermediates. Productive pathways in the solution-processed SC fabrication are shown as bold arrows. (a) DMSO-mediated pathways as studied for free-standing crystals, except for steps i–iii (also steps xv and xvi) performed in solution. Detailed conditions are shown in Figures S1–S3. (b) Optical microscopic image of an **INT-3** fiber on a loop for in situ X-ray diffraction (XRD) experiments. (c) DMF-mediated pathways. (d) SEM image of a brittle **PV** fiber obtained by heating **INT-7**.

bridged, square bipyramidal $(PbI_2)_n$ polymer chain (Figure 4a–e,j,k).[26] The $(PbI_3^-)_2PbI_2$ structure in **INT-3** is stabilized by a hydrogen-bonded network of MA^+·DMSO (Figure 4e). **INT-7** is similarly arranged in the crystal (Figure 4k).

The very facile conversion of **PV** back to **INT-3** (step x) suggests their topological similarity, which we can identify by superimposing the crystal structure of **INT-3** on the cubic lattice of **PV**[15] (Figure 4, middle panel). Here, we see that the motion of each trinuclear plumbate in a pair along the red arrow directions converts **INT-3** (Figure 4g) to **PV** or vice versa (Figure 4h,i; see Figure 1 for the experimental crystal structure of **PV** on which Figure 4h,i was drawn). In this way, the polymer strips of **INT-3** laid along the fiber axis are zipped together to form a cubic **PV** crystal with minimum atomic motions (Figure 2a–f). In the reverse process, which occurs quickly at 25 °C, DMSO extracts MAI from the cubic PbI_3^- lattice of **PV** to form MA^+·DMSO hydrogen bonded to the trinuclear $(PbI_3^-)_2PbI_2$ of **INT-3**. The same applies to the correlation between **INT-7** and **PV** shown in Figure 4l–n. These processes accompany rotation of the crystal *a*-axis lattice of **INT-3** by ca. 45°, which was experimentally verified by 2-D XRD analysis, as described next.

2-D XRD Analysis of Interconversion between Intermediates and PV. Experimental evidence for the 45° rotation was provided by 2-D XRD analysis of free-standing fibers (cf. Figure 3b), which also allowed us to in situ study the **PV** crystal annealing process (Figure 5a–d for DMSO and Figure 5e–h for DMF). Figure 5a shows a 2-D XRD image of several parallel fibers of the plumbate **INT-3**, where (002), (021), and (022) diffractions are aligned linearly, indicating that the 1-D polymer axis (crystal *a*-axis) is parallel to the fiber axis. The **PV** fiber obtained by first heating **INT-3** (DMSO) in Figure 5b shows six spots on the (100) circle, two on the horizontal line and four with 45° inclination. Thus, as shown in the inset (Figure 5b), the (110) normal runs parallel to the fiber axis (Figure 4i), leaving two of the axes to make 45° and the other 90° angles to the fiber axis.

Crystal annealing was examined next. Heating at 100 °C converted **INT-3** to **PV** (Figure 5b). Sequential treatment of the **PV** fibers with DMSO vapor at 25 °C and with heating at 100 °C regenerated first partially oriented **INT-3** (Figure 5c) and then **PV** that shows random crystal orientation (Figure 5d). Figure 2i illustrates such randomness. Regenerated **INT-3** shows an interesting feature; the **INT-3** crystals have grown mainly in a direction orthogonal to the fiber axis (cf. Figure 5c vs 5a); that is, the crystals grew from the surface toward the center, as DMSO molecules diffused from the surface.

Similarly to DMSO, in Figure 5e for **INT-7** from DMF, we see that the 1-D polymer axis (crystal *a*-axis) is also parallel to the fiber axis. However, Figure 5f shows two additional spots at upper and bottom tangential positions, indicating that it is a ca. 1:1 mixture of crystals (inset) whose (110) normal runs both parallel and orthogonal to the fiber axis. As to the crystal annealing, heating/DMF-annealing of **INT-7** rapidly randomize the crystal orientation (Figure 5h), indicating that DMF is an effective solvent for production of polycrystalline **PV** powder.

We consider that the difference in the crystal volume change during conversion of **INT-3** or **INT-7** into **PV** affects the crystal quality of **PV** fibers. **INT-3** takes one MAI and loses two DMSO molecules to produce **PV** (steps vii–ix), resulting in

DOI: 10.1021/jacs.5b10599
J. Am. Chem. Soc. 2015, 137, 15907–15914

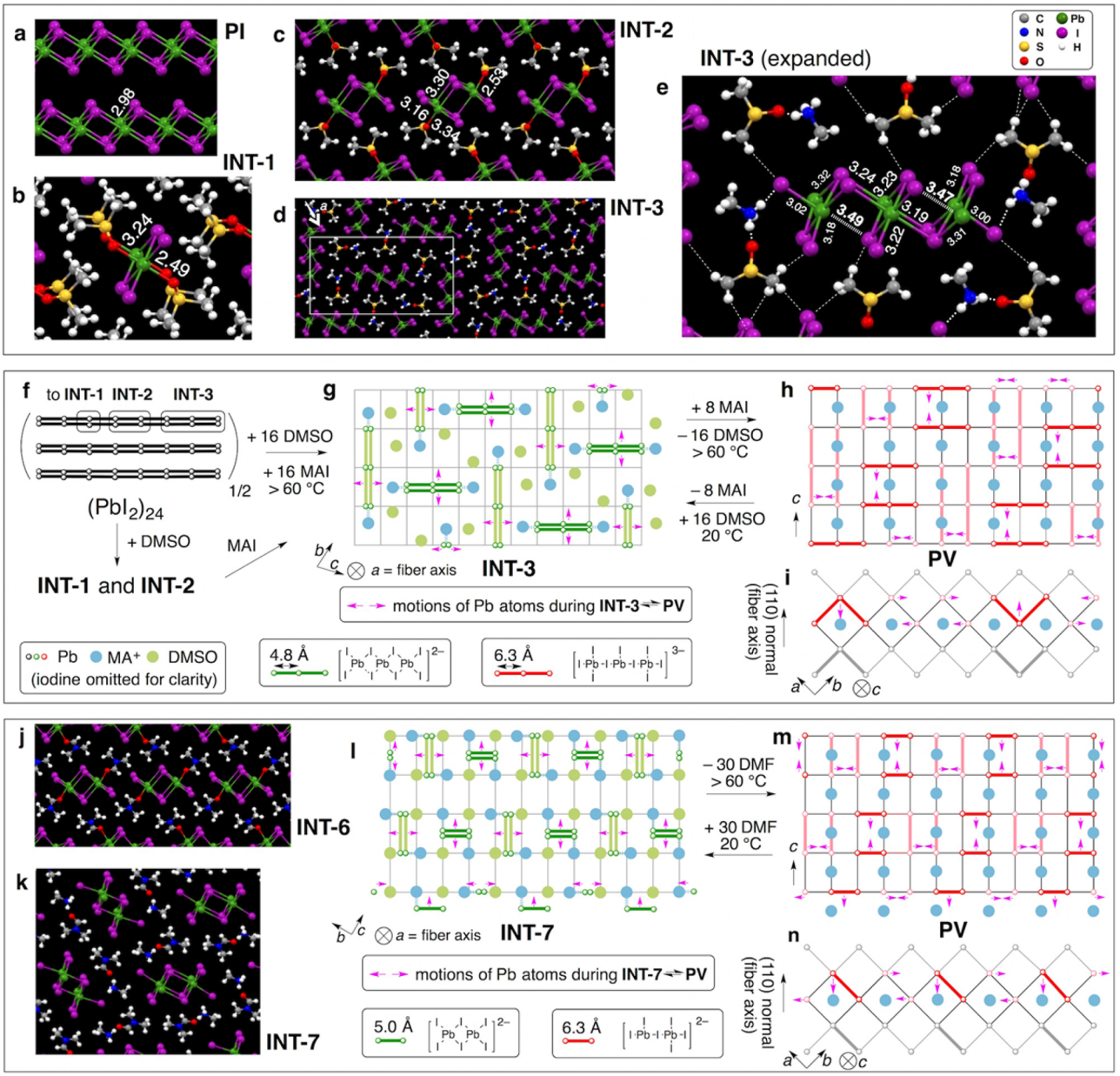

Figure 4. Crystal structures of intermediates and their interconversions. Only two Pb sequences are shown for clarity. Atomic distances are in angstroms in crystallographic structures. The structures of **INT-2** and -**3** were determined in this study. (Top panel) (a) **PI** (ref 25); (b) **INT-1**; (c) **INT-2**; (d) **INT-3** seen approximately along the *a*-axis (=fiber axis), where a = 4.6216(7) Å, b = 27.455(4) Å, c = 26.933(4) Å, and $\alpha = \beta = \gamma = 90°$; and (e) **INT-3**. (Middle panel) (f) Topological illustration on going from **PI** to **INT-1** to **INT-3**; (g) **INT-3** in panel d projected onto the cubic lattice of **PV** in panel h, where the polymer chains extend along the *a*-axis perpendicular to the plane of the paper and trinuclear strips move along the red arrows to form **PV**; (h) **PV** crystal lattice correlated to **INT-3** in panel g, where red arrows illustrate conversion to **INT-3**; and (i) top view of panel h, where the (110) normal = the *a*-axis of **INT-3** (=the fiber axis). (Bottom panel) (j) **INT-6** (ref 20); (k) **INT-7** (ref 21); (l) **INT-7** in panel k projected onto the crystal lattice of **PV** in panel m; (m) **PV** crystal lattice correlated to **INT-7** in panel l; and (n) top view of panel m, where the (110) normal = the *a*-axis of **INT-7**.

only 13% decrease of the crystal volume (from 285 to 247 Å^3/Pb at 20 °C). On the other hand, **INT-7** loses two DMF molecules to produce **PV** (step xviii), resulting in a 30% decrease (from 354 to 247 Å^3/Pb at 20 °C).

Temperature-dependent in situ 1-D XRD analysis tells us the time-course of the DMSO-mediated reaction (Figure 5i,j). As the ambient nitrogen temperature was increased from 20 to 130 °C, **INT-3** coated with MAI changes to **PV** in three stages via **INT-4** (2θ = 5.7°) and **INT-5** (2θ = 7.9°) (Figure S8, SI). The decrease of the smallest 2θ value of 6.6° in **INT-3** to 5.7° in **INT-4** (i.e., spacing increase of ca. 0.21 nm) suggests an MAI uptake as the first step at >30 °C, followed by loss of one DMSO molecule to form **INT-5** and another to form **PV**. In contrast, the dinuclear plumbate **INT-7** loses DMF molecules at >50 °C and produces **PV** in a single step (Figure 5k,l).

Photovoltaic Device and Photodetectors. We describe finally that this oriented **PV** fiber made from **INT-3** shows excellent optoelectronic properties as examined for photovoltaic (Figure 6a and Figure S9, SI). Made entirely free from solvent, this fiber exhibits a high chemical stability and ohmic contact with gold electrodes and optoelectronic properties comparable to a single-block crystal. In contrast, the **PV** fiber

DOI: 10.1021/jacs.5b10599
J. Am. Chem. Soc. 2015, 137, 15907–15914

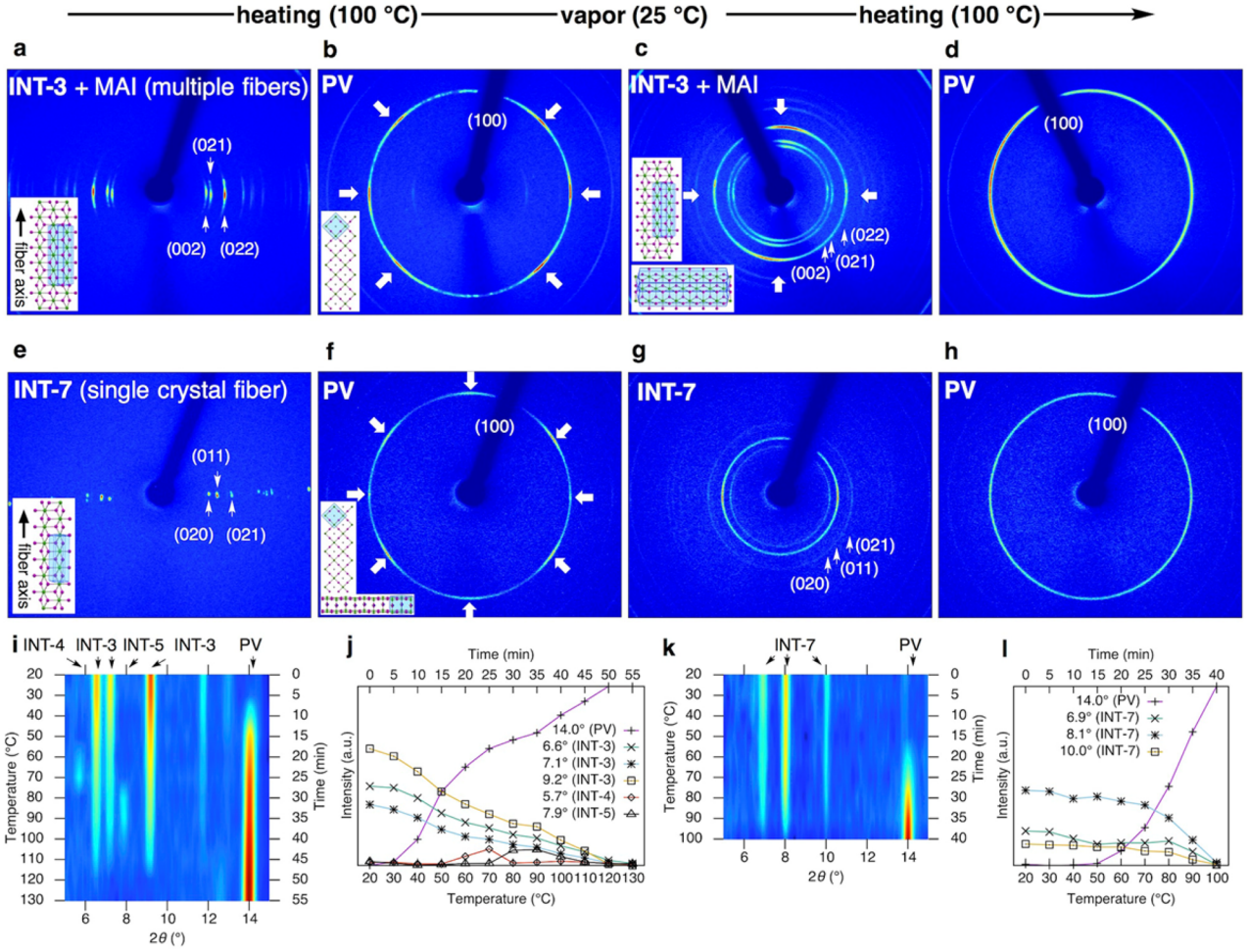

Figure 5. Fiber XRD analyses of sequential conversion of **INT-3** or -7 to **PV**. The reaction of a bundle of several fibers coated with MAI (inset: lattice orientation in the fiber and BFDH (Bravais, Friedel, Donnay, and Harker) simulated crystal morphology in blue): (a) **INT-3** at 20 °C, (b) **PV** at 100 °C after heating **INT-3** at 100 °C, (c) **INT-3** at 20 °C obtained by exposure of **PV** to DMSO vapor, and (d) **PV** at 100 °C after heating **INT-3** at 100 °C. The reactions of a single fiber of **INT-7**: (e) **INT-7** at 20 °C, (f) 2-D XRD image of **PV** at 100 °C after heating **INT-7** at 100 °C, (g) **INT-7** at 20 °C by exposure of **PV** to DMF vapor, and (h) **PV** at 100 °C after heating **INT-7** at 100 °C. (i) Change of XRD signal intensity (2θ = 5°−15°) during **INT-3**−**PV** conversion (measured every 10 °C, which was maintained for 5 min). (j) Time lapse of XRD signal intensity for the data in panel i, revealing the intermediacy of **INT-4** (red line, 2θ = 5.7°) and **INT-5** (black line, 2θ = 7.9°). (k) The same data as panel l for **INT-7**−**PV** conversion. (l) Time lapse of XRD signal intensity for the data in panel k.

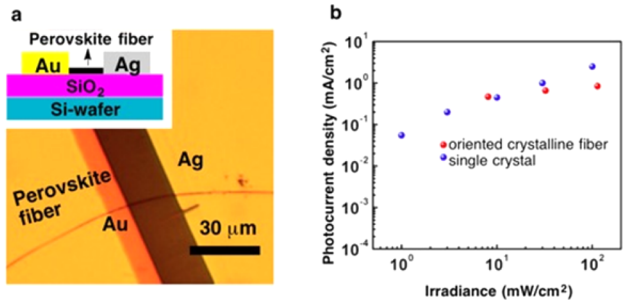

Figure 6. Lateral device using submicron PV fiber and device characteristics. (a) Optical microscopic image of a photovoltaic device using a single **PV** fiber, which is protected by a CYTOP film of 500 nm thickness (fiber width is 0.4 μm and channel width 25 μm). Inset: schematic device structure. (b) Photocurrent density of the **PV** fiber device (red) compared with a device using a 200 μm-thick single-block crystal of **PV** (blue, ref 11).

annealed under DMSO vapor exposure hardly maintains its structural integrity for device applications (cf. Figure 2i), indicating that quality control of the **PV** fiber is a worthwhile future task for realization of **PV**-based microdevices. Figure 6b indicates that the photocurrent density of the fiber device (red) is comparable with that of a 200-μm-thick perovskite block-crystal device reported recently (blue).[11]

We describe the photovoltaic devices in some detail. We transferred a single fiber of **INT-3** onto a silicon wafer covered with a SiO_2 layer (470 nm), heated them at 130 °C for 10 min under nitrogen, and finally vacuum deposited Au (50 nm) and Ag (100 nm) on fibers separated from each other by 25 μm. We stabilized the device by spin-coating with CYTOP followed by heating at 100 °C for 30 min in N_2. The characteristics of these devices were determined under irradiation with different light intensities. The **PV** fiber device shows a power conversion efficiency (PCE) of 1.35% (average 1.27%) at a light power of 8.1 mW/cm^2 with a short-circuit current density (J_{sc}) of 0.567 mA/cm^2, an open-circuit voltage (V_{oc}) of 0.65 V, and a fill factor (FF) of 29.7%. Since the fiber is thin (ca. 500 nm), its contact with the electrodes is limited and the photocurrent gradually saturated under high-power light irradiance.

DOI: 10.1021/jacs.5b10599
J. Am. Chem. Soc. 2015, 137, 15907−15914

We also fabricated a photodetector on a silicon wafer covered with a SiO_2 layer by depositing two parallel 100-nm-thick Au electrodes over a single PV nanofiber followed by coating with a film of CYTOP[27] (see details in the Experimental Section). The observed linearity of the current−voltage curve at different light powers indicated ohmic contact between the nanofibers and gold electrodes (Figure 7). The device was found to show respectable responsivities of 1.1 A/W at 8.1 mW/cm^2 and 0.23 A/W at 194.1 mW/cm^2.

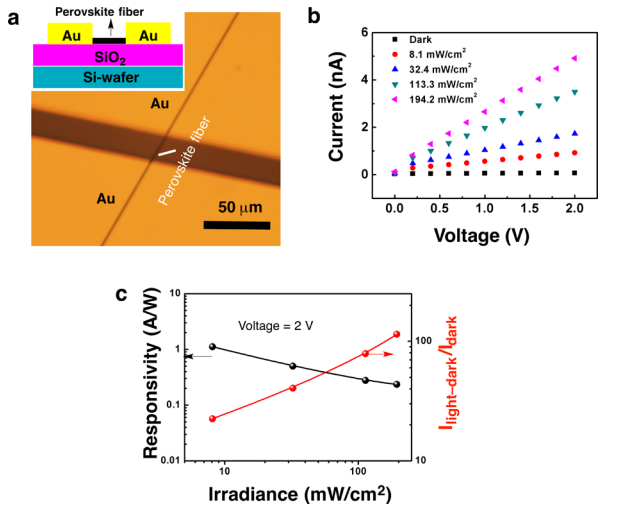

Figure 7. Details of the single-fiber photodetector. (a) Photodetector using a single **PV** fiber (the width of fiber is 0.5 μm and fiber length in channel is 24 μm). Inset: schematic device structure. Before testing, the device was protected by coating with CYTOP. (b) The current response of the photodetector based on perovskite fiber under different irradiance. (c) Responsivity and photocurrent/dark current ratios versus irradiance of the photodetectors.

CONCLUSION

We have elucidated the crystal-to-crystal basis of various pathways connecting **PI** and **PV** in the presence of MAI and DMSO or DMF, polar solvents used widely for solution-processed **PV** SC devices. The reaction is driven by reversible participation of the solvent molecules and involves conversion of a 2-D sheet crystal of **PI** first to 1-D polymeric strips of PbI_2 and PbI_3^- oligomers and then to a 3-D cubic **PV** crystal. Mobile equilibria among various chemical species are established under 100 °C until the solvent is lost from the system by evaporation. The extreme facility of reversion of **PV** back to plumbate intermediates such as **INT-3** and **7**, occurring even at room temperature, is a particularly problematic step from the context of device fabrication and probably accounts for the irreproducibility of device fabrication and the lack of device longevity. This reversibility between **PV** and the plumbate intermediates, however, is indispensible for the growth of the initially formed **PV** fibrous crystals into larger of **PV** crystals required for high-performance SC devices. Temperatures higher than 130 °C regenerate **PI** by loss of MAI from **PV**, providing another pathway of SC device degradation. DMSO and DMF play essentially the same role throughout the reaction: conversion of 2-D PbI_2 sheet to 2-D strips (**INT-1** and **INT-6**) and stabilization of plumbate crystals through hydrogen bonding to the MA^+ molecules (e.g., Figure 4e). Solvent choice is critical, however, because different solvents cause different crystallographic conversions (Figure 5) and, hence, affect the morphology and stability of intermediates. As a consequence, DMSO but not DMF produces oriented crystalline **PV** fibers that serve as a stable and high-performance active material for miniature optoelectronic devices, such as photovoltaic and photodetecting devices.

EXPERIMENTAL SECTION

Materials. PbI_2 (99.999% purity) was purchased from Strem Chemicals, Inc. and used without further purification. MAI was prepared by using the procedure reported in ref 2.

Preparation of INT-1 [mononuclear strips of $(PbI_2)_n$, PbI_2·$DMSO_2$]. A 30 wt % PbI_2 solution was prepared by adding PbI_2 (448 mg) to DMSO/γ-butyrolactone (GBL) (1.0 mL, 3:7 vol/vol ratio) and it stirred for 12 h at 60 °C. The solution was then cooled to room temperature to obtain crystals of **INT-1**.

Preparation of INT-2 [dinuclear strips of $(PbI_2)_n$, $(PbI_2)_2$·$DMSO_2$]. A 40 wt % PbI_2/MAI solution was prepared by adding PbI_2 (555 mg) and MAI (192 mg) in DMSO/GBL (1.0 mL, 3:7 vol/vol ratio) and it stirred for 12 h at 60 °C. The solution was cooled to room temperature, and 10−20 vol % of toluene was added to obtain fibers of **INT-2**.

Preparation of INT-3 [trinuclear strips of $(PbI_2)_n$ coordinated by two iodide ions, $(MA^+)_2[(PbI_3^-)_2PbI_2]$·$DMSO_2$]. A 50 wt % PbI_2/MAI solution was prepared by adding PbI_2 (833 mg) and MAI (287 mg) in DMSO/GBL (1.0 mL, 3:7 vol/vol ratio) and it stirred for 12 h at 60 °C. The solution was cooled to room temperature to obtain fibers of **INT-3**.

Preparation of INT-6 [dinuclear strips of $(PbI_2)_n$, $(PbI_2)_2$·DMF_2]. A 30 wt % PbI_2 solution was prepared by adding PbI_2 (405 mg) to DMF (1.0 mL) and it stirred for 12 h at 60 °C. The solution was then cooled to room temperature to obtain fibers of **INT-6**.

Preparation of INT-7 [dinuclear strips of $(PbI_2)_n$ coordinated by two iodide ions, $(MA^+)_2(PbI_3^-)_2$·DMF_2]. A 50 wt % PbI_2/MAI solution was prepared by adding PbI_2 (702 mg) and MAI (242 mg) in DMF (1.0 mL) and it stirred for 12 h at 60 °C. The solution was cooled to room temperature to obtain fibers of **INT-7**.

Crystallographic Analysis of Single Crystals INT-1−3. The diffraction images for X-ray crystallographic analysis were collected on a Rigaku Rapid II diffractometer equipped with an imaging plate (IP) using Cu Kα (λ = 1.5419 Å) radiation. For crystallographic analysis, the sample was removed from the mother liquor and put onto a glass slide. A crystal was chosen and then it was put on and taken off from a glass slide several times to remove liquid from its surface.

The supplementary crystallographic data for this paper were deposited with the Cambridge Crystallographic Data Centre (CCDC), as nos. 1063982, 1063983, 1064049, 1415480, and 1415481. These data can be obtained free of charge from CCDC via www.ccdc.cam.ac.uk/data_request/cif.

Fiber XRD Diffraction Analyses. The diffraction images for fiber X-ray analyses were collected on a Rigaku Rapid II diffractometer equipped with an IP using Cu Kα (λ = 1.5419 Å) radiation. Diffraction images were taken under the following conditions: exposure time, 1 s/deg; dω, 180°. The fiber was placed with its fiber axis perpendicular to the horizontal line. The fiber was kept under nitrogen atmosphere during measurement. A heater attached to the nitrogen generator controlled the temperature. Image acquisition took 5 min (3 min for exposure, 2 min for IP reading).

For the fibers coated with MAI and DMSO, first, a bundle of fibers was removed from the mother liquor by tweezers and put on a glass slide. Then a sample loop was used to pick up multiple fibers without removing liquid from their surface, and the fibers were mounted on a goniometer.

For fibers without MAI and DMSO, first, a sample loop was used to pick up a single fiber. To remove liquid from the surface, the fiber was dipped into a droplet of dichloromethane and then mounted on a goniometer.

The conversion from **INT-3** to **PV** was performed in the following manner. **INT-2** fibers were put on a glass slide without removing the

DOI: 10.1021/jacs.5b10599
J. Am. Chem. Soc. 2015, 137, 15907−15914

solvent surrounding them. The sample was left under ambient conditions until most of the solvent evaporated (for 2 h) to obtain **INT-3** fibers covered with MAI. A bundle of fibers aligned in the same direction was then taken by a sample loop and mounted on a goniometer. **INT-3** fibers were heated from 20 to 100 °C with an interval of 5 min for each 10 °C. Conversion to **PV** was completed around 0.5 h after the temperature reached 100 °C. The conversion quickly finished at 130 °C.

The conversion from **INT-7** to **PV** was studied in a similar manner as for **INT-3**−**PV** conversion. **INT-7** fibers were prepared directly from solution. A single **INT-7** fiber was heated from 20 to 100 °C with an interval of 5 min for each 10 °C. The conversion completed when the temperature reached 100 °C.

For the vapor-treatment experiment, the **PV** fiber sample was prepared from **INT-3** or **INT-7** as described above. The **PV** fiber sample was kept for 0.5 h under nitrogen saturated with DMSO or DMF vapor. The fiber XRD measurement was performed at 20 °C. Conversion to **PV** finished at 100 °C.

Preparation of Photovoltaic Device and Photodetector. A lateral photovoltaic device or photodetector using PV fiber was fabricated on a silicon wafer covered with a SiO_2 layer (470 nm). Two parallel asymmetric (Au and Ag) or symmetric (Au only) metal electrodes were vacuum-deposited on a single **PV** fiber made from an **INT-3** fiber (without washing) heating at 130 °C/10 min. A MAX-303 xenon lamp (VIS) light source from ASAHI SPECTRA illuminated the photovoltaic device and photodetector from the top of the device. The value of photocurrent density in Figure 6 refers to the short circuit current density of the device.

The photodetector showed respectable photoresponse characteristics, working at a voltage below 2 V with a dark current of 0.04 nA. Responsivity (R) was calculated by following the equation

$$R = (I_{light} - I_{dark})/P_{light} \quad (1)$$

where I_{light} is photocurrent in amperes, I_{dark} is the dark current in amperes, and P_{light} is the incident light power in watts [P_{light} = irradiance × S, where S is the area of active materials ($S = WL$, where W is the width of the fiber and L is the length between two electrodes)].

■ ASSOCIATED CONTENT

Supporting Information

The Supporting Information is available free of charge on the ACS Publications website at DOI: 10.1021/jacs.5b10599.

Details of XRD analysis and device fabrication (PDF)
Crystallographic data for **INT-1** in CIF format (CIF)
Crystallographic data for **INT-2** (−150 °C) in CIF format (CIF)
Crystallographic data for **INT-2** (20 °C) in CIF format (CIF)
Crystallographic data for **INT-3** (−150 °C) in CIF format (CIF)
Crystallographic data for **INT-3** (20 °C) in CIF format (CIF)

■ AUTHOR INFORMATION

Corresponding Author

*nakamura@chem.s.u-tokyo.ac.jp

Author Contributions

Y.G. and K.S. contributed equally to this work.

Notes

The authors declare no competing financial interests.

■ ACKNOWLEDGMENTS

We thank MEXT for financial support [KAKENHI 15H05754 and CREST, JST to E.N., and "Nanotechnology Platform" (No. 12024046)]. Y.G. thanks Strategic Promotion of Innovative Research, JST; K.S. thanks the Japan Society for the Promotion of Science for Leading Graduate Schools (MERIT); and K.I. thanks the Advanced Leading Graduate Course for Photon Science (ALPS).

■ REFERENCES

(1) Kojima, A.; Teshima, K.; Shirai, Y.; Miyasaka, T. *J. Am. Chem. Soc.* **2009**, *131*, 6050−6051.
(2) Lee, M. M.; Teuscher, J.; Miyasaka, T.; Murakami, T. N.; Snaith, H. J. *Science* **2012**, *338*, 643−647.
(3) Zhou, H.; Chen, Q.; Li, G.; Luo, S.; Song, T. B.; Duan, H. S.; Hong, Z.; You, J.; Liu, Y.; Yang, Y. *Science* **2014**, *345*, 542−546.
(4) Tan, Z.-K.; Moghaddam, R. S.; Lai, M. L.; Docampo, P.; Higler, R.; Deschler, F.; Price, M.; Sadhanala, A.; Pazos, L. M.; Credgington, D.; Hanusch, F.; Bein, T.; Snaith, H. J.; Friend, R. H. *Nat. Nanotechnol.* **2014**, *9*, 687−692.
(5) Xing, G.; Mathews, N.; Lim, S. S.; Yantara, N.; Liu, X.; Sabba, D.; Grätzel, M.; Mhaisalkar, S.; Sum, T. C. *Nat. Mater.* **2014**, *13*, 476−480.
(6) Zhu, H.; Fu, Y.; Meng, F.; Wu, X.; Gong, Z.; Ding, Q.; Gustafsson, M. V.; Trinh, M. T.; Jin, S.; Zhu, X. Y. *Nat. Mater.* **2015**, *14*, 636−642.
(7) Burschka, J.; Pellet, N.; Moon, S.-J.; Humphry-Baker, R.; Gao, P.; Nazeeruddin, M. K.; Grätzel, M. *Nature* **2013**, *499*, 316−319.
(8) Jeon, N. J.; Noh, J. H.; Yang, W. S.; Kim, Y. C.; Ryu, S.; Seo, J.; Seok, S. I. *Nature* **2015**, *517*, 476−480.
(9) (a) Zuo, L.; Gu, Z.; Ye, T.; Fu, W.; Wu, G.; Li, H.; Chen, H. *J. Am. Chem. Soc.* **2015**, *137*, 2674−2679. (b) Li, X.; Ibrahim Dar, M.; Yi, C.; Luo, J.; Tschumi, M.; Zakeeruddin, S. M.; Nazeeruddin, M. K.; Han, H.; Grätzel, M. *Nat. Chem.* **2015**, *7*, 703−711.
(10) Kim, J. H.; Williams, S. T.; Cho, N.; Chueh, C.-C.; Jen, A. K. Y. *Adv. Energy Mater.* **2015**, *5*, DOI:10.1002/aenm.201401229
(11) Dong, Q.; Fang, Y.; Shao, Y.; Mulligan, P.; Qiu, J.; Cao, L.; Huang, J. *Science* **2015**, *347*, 967−970.
(12) Horváth, E.; Spina, M.; Szekrényes, Z.; Kamarás, K.; Gaal, R.; Gachet, D.; Forró, L. *Nano Lett.* **2014**, *14*, 6761−6766.
(13) Deng, H.; Dong, D.; Qiao, K.; Bu, L.; Li, B.; Yang, D.; Wang, H.-E.; Cheng, Y.; Zhao, Z.; Tang, J.; Song, H. *Nanoscale* **2015**, *7*, 4163−4170.
(14) Xing, J.; Liu, X. F.; Zhang, Q.; Ha, S. T.; Yuan, Y. W.; Shen, C.; Sum, T. C.; Xiong, Q. *Nano Lett.* **2015**, *15*, 4571−4577.
(15) Stoumpos, C. C.; Malliakas, C. D.; Kanatzidis, M. G. *Inorg. Chem.* **2013**, *52*, 9019−9038.
(16) Onoda-Yamamuro, N.; Matsuo, T.; Suga, H. *J. Phys. Chem. Solids* **1990**, *51*, 1383−1395.
(17) (a) Tang, Q. X.; Li, H. X.; Liu, Y. L.; Hu, W. P. *J. Am. Chem. Soc.* **2006**, *128*, 14634−14639. (b) Seiki, N.; Shoji, Y.; Kajitani, T.; Ishiwari, F.; Kosaka, A.; Hikima, T.; Takata, M.; Someya, T.; Fukushima, T. *Science* **2015**, *348*, 1122−1126.
(18) Shi, D.; Adinolfi, V.; Comin, R.; Yuan, M.; Alarousu, E.; Buin, A.; Chen, Y.; Hoogland, S.; Rothenberger, A.; Katsiev, K.; Losovyj, Y.; Zhang, X.; Dowben, P. A.; Mohammed, O. F.; Sargent, E. H.; Bakr, O. M. *Science* **2015**, *347*, 519−522.
(19) Miyamae, H.; Numahata, Y.; Nagata, M. *Chem. Lett.* **1980**, *9*, 663−664.
(20) Wakamiya, A.; Endo, M.; Sasamori, T.; Tokitoh, N.; Ogomi, Y.; Hayase, S.; Murata, Y. *Chem. Lett.* **2014**, *43*, 711−713.
(21) Hao, F.; Stoumpos, C. C.; Liu, Z.; Chang, R. P. H.; Kanatzidis, M. G. *J. Am. Chem. Soc.* **2014**, *136*, 16411−16419.
(22) Møller, C. K. *Nature* **1958**, *182* (4647), 1436−1436.
(23) Chung, I.; Song, J.-H.; Im, J.; Androulakis, J.; Malliakas, C. D.; Li, H.; Freeman, A. J.; Kenney, J. T.; Kanatzidis, M. G. *J. Am. Chem. Soc.* **2012**, *134* (20), 8579−8587.
(24) Jeon, N. J.; Noh, J. H.; Kim, Y. C.; Yang, W. S.; Ryu, S.; Seok, S. I. *Nat. Mater.* **2014**, *13* (9), 897−903.
(25) Terpstra, P.; Westenbrink, H. G. *Proc. Koninklijke Nederlandse Academie van Wetenschappen* **1926**, *29*, 431−442.
(26) Beckmann, P. A. *Cryst. Res. Technol.* **2010**, *45*, 455−460.

DOI: 10.1021/jacs.5b10599
J. Am. Chem. Soc. 2015, 137, 15907−15914

(27) Guo, Y.; Liu, C.; Tanaka, H.; Nakamura, E. *J. Phys. Chem. Lett.* **2015**, *6*, 535−539.

DOI: 10.1021/jacs.5b10599
J. Am. Chem. Soc. 2015, 137, 15907−15914